tion, even at time scales shorter than the vibration frequency, f. In equilibrium, the mean kinetic energies associated with the two in-plane translation degrees of freedom of the particle are equal, by the equipartition theorem, even if the particle shape is anisotropic. Figure 3 is a histogram of the magnitude of particle displacements over a time corresponding to the camera frame rate [1/300 s, or $(2/3)f^{-1}$]. The displacement along and perpendicular to the axis of the rod are displayed separately, showing that a particle is about 2.3 times as likely to move along its length as it is to move transverse to its length. Because the period of the imposed vibration (f^{-1}) sets the scale for the mean free time of the particles, this shows that the motion of the rods is anisotropic even at time scales less than or comparable to the mean free time between collisions.

We have thus presented an experimental demonstration of giant, long-lived number fluctuations in a two-dimensional active nematic. The particles in our driven system do not communicate except by contact, have no sensing mechanisms, and are not influenced by the spatially varying pressures and incentives of a biological environment. This reinforces the view that, in living matter as well, simple, nonspecific interactions can give rise to large spatial inhomogeneity. Equally important, these effects offer a counterexample to the deeply held notion that density is a sharply defined quantity for a large system.

References and Notes

1. T. Vicsek, A. Czirok, E. Ben-Jacob, I. Cohen, O. Shochet, *Phys. Rev. Lett.* **75**, 1226 (1995).
2. J. Toner, Y. Tu, *Phys. Rev. Lett.* **75**, 4326 (1995).
3. J. Toner, Y. Tu, *Phys. Rev. E* **58**, 4828 (1998).
4. J. Toner, Y. Tu, S. Ramaswamy, *Ann. Phys.* **318**, 170 (2005).
5. S. Ramaswamy, R. A. Simha, J. Toner, *Europhys. Lett.* **62**, 196 (2003).
6. C. Holden, *Science* **313**, 779 (2006).
7. J. Buhl *et al.*, *Science* **312**, 1402 (2006).
8. N. C. Makris *et al.*, *Science* **311**, 660 (2006).
9. C. Becco *et al.*, *Physica A (Amsterdam)* **367**, 487 (2006).
10. B. Szabó *et al.*, *Phys. Rev. E* **74**, 061908 (2006).
11. F. Nédélec, T. Surrey, A. C. Maggs, S. Leibler, *Nature* **389**, 305 (1997).
12. D. Bray, *Cell Movements: From Molecules to Motility* (Garland, New York, 2001).
13. H. Gruler, U. Dewald, M. Eberhardt, *Eur. Phys. J. B* **11**, 187 (1999).
14. V. Narayan, N. Menon, S. Ramaswamy, *J. Stat. Mech.* **2006**, P01005 (2006).
15. H. Chaté, F. Ginelli, R. Montagne, *Phys. Rev. Lett.* **96**, 180602 (2006).
16. A. Prevost, D. A. Egolf, J. S. Urbach, *Phys. Rev. Lett.* **89**, 084301 (2002).
17. P. M. Reis, R. A. Ingale, M. D. Shattuck, *Phys. Rev. Lett.* **96**, 258001 (2006).
18. J. Galanis, D. Harries, D. L. Sackett, W. Losert, R. Nossal, *Phys. Rev. Lett.* **96**, 028002 (2006).
19. Materials and methods are available on *Science* Online.
20. D. L. Blair, T. Neicu, A. Kudrolli, *Phys. Rev. E* **67**, 031303 (2003).
21. I. Aranson, D. Volfson, L. S. Tsimring, *Phys. Rev. E* **75**, 051301 (2007).
22. W. Feller, *An Introduction to Probability Theory and its Applications* (Wiley, New York, ed. 3, 2000), vol. I.
23. A. Ahmadi, T. B. Liverpool, M. C. Marchetti, *Phys. Rev. E* **74**, 061913 (2006).

24. We thank V. Kumaran, P. Nott, and A. K. Raychaudhuri for generously letting us use their experimental facilities. V.N. thanks S. Kar for help with some of the experiments. V.N. and S.R., respectively, thank the Council for Scientific and Industrial Research, India, and the Indo-French Centre for the Promotion of Advanced Research (grant 3504-2) for support. The Centre for Condensed Matter Theory is supported by the Department of Science and Technology, India. N.M. acknowledges financial support from NSF under grants DMR 0606216 and 0305396.

Supporting Online Material

www.sciencemag.org/cgi/content/full/317/5834/105/DC1
Materials and Methods
SOM Text
Figs. S1 to S6
Movies S1 and S2

25 January 2007; accepted 31 May 2007
10.1126/science.1140414

Trench-Parallel Anisotropy Produced by Foundering of Arc Lower Crust

Mark D. Behn,[1]* Greg Hirth,[1] Peter B. Kelemen[2]

Many volcanic arcs display fast seismic shear-wave velocities parallel to the strike of the trench. This pattern of anisotropy is inconsistent with simple models of corner flow in the mantle wedge. Although several models, including slab rollback, oblique subduction, and deformation of water-rich olivine, have been proposed to explain trench-parallel anisotropy, none of these mechanisms are consistent with all observations. Instead, small-scale convection driven by the foundering of dense arc lower crust provides an explanation for the trench-parallel anisotropy, even in settings with orthogonal convergence and no slab rollback.

The origin of seismic anisotropy in Earth's upper mantle is attributed to the deformation-induced alignment of olivine crystals. Anisotropy can be quantified through measurements of shear-wave splitting, in which the orientation and strength of the anisotropy are estimated by measuring the polarization direction of the fastest-propagating shear wave and the delay time between the arrivals of the fastest and slowest shear waves. The relation between anisotropy and mantle flow is seen clearly at mid-ocean ridges, where fast polarization directions are oriented parallel to the spreading direction (*1*). This observation is consistent with a model in which the olivine *a* axis aligns with the transport direction inferred for corner flow beneath a ridge (*2*, *3*).

Beneath volcanic arcs, shear-wave splitting measurements frequently show fast polarization directions parallel to the strike of the arc (*4*–*6*), which rotate to a trench-normal orientation in the back-arc (*5*, *6*). Direct comparison of delay times from teleseismic *SKS* phases (which propagate through the entire mantle) (*7*) and local *S* phases generated in the subducting slab (*8*) indicates that a substantial fraction of the trench-parallel anisotropy resides in the mantle wedge above the slab (Fig. 1). Splitting measurements from local events also show strong along-arc variability in the orientation of anisotropy, with certain regions being characterized by trench-parallel anisotropy and other regions displaying more variable fast polarization directions (Fig. 1) (*8*–*10*). In contrast, two-dimensional (2D) models of slab-driven corner flow, like those invoked to explain the pattern of anisotropy at mid-ocean ridges, predict trench-normal anisotropy in the mantle wedge at subduction zones (*11*).

Deformation experiments on olivine aggregates show that the lattice preferred orientation (LPO) changes as a function of water content, stress, and temperature (*12*, *13*). Particularly intriguing is the observation of LPO controlled by the dominance of slip on the (010)[001] slip system (i.e., the B-type system). In this regime, which is predicted to dominate at high water content and low temperature/high stress, fast polarization directions are perpendicular to the flow direction (they are trench-parallel for 2D slab-driven corner flow). However, although numerical models (*14*) predict B-type fabric in the fore-arc, it is not predicted beneath the arc or in the back-arc, where trench-parallel anisotropy is often observed.

An alternative explanation for trench-parallel anisotropy is 3D flow in the mantle wedge due to oblique convergence or slab rollback (*11*, *15*). Yet, these models do not explain trench-parallel anisotropy observed in settings with nearly orthogonal convergence and little rollback (Fig. 1) (*4*, *8*). Another potential source of 3D flow in the mantle wedge is buoyancy-driven flow resulting from the foundering of high-density mafic and ultramafic cumulates into the underlying mantle (*16*). At conditions appropriate for arc lower crust (800° to 1000°C and 1 GPa) (*17*), many crustal

[1]Department of Geology and Geophysics, Woods Hole Oceanographic Institution, Woods Hole, MA 02543, USA. [2]Lamont Doherty Earth Observatory, Columbia University, Palisades, NY 10964, USA.

*To whom correspondence should be addressed. E-mail: mbehn@whoi.edu

assemblages are denser than the underlying mantle (*16*, *18*, *19*). Such high-density layers can become gravitationally unstable and sink into the mantle with a characteristic along-arc spacing of 30 to 50 km on time scales of ~10^6 years (fig. S1) (*18*).

Here we show that 3D flow in the mantle wedge due to lower-crustal foundering is capable of producing trench-parallel seismic anisotropy. We used finite element models to calculate instantaneous mantle flow beneath an idealized island arc [Fig. 2A and supporting online material (SOM)]. We assumed an asthenospheric viscosity of 3×10^{18} Pa·s, which is consistent with the extrapolation of experimental data to mantle wedge conditions in the presence of water and/or melt (*20*). To promote corner flow similar to that produced with temperature-dependent and/or stress-dependent viscosity (*17*, *21*), we imposed zero coupling between the downgoing slab and the lithosphere and a shallowing of the lithosphere/asthenosphere boundary directly beneath the arc (Fig. 2A).

We analyzed instantaneous flow induced by a series of spheres 16 km in diameter, located at a depth of 50 km (~20 km below the crust/mantle transition) and with an along-arc spacing of 40 km (Fig. 2A). The size and spacing of the instabilities were based on the scaling analysis and geochemical modeling of the Talkeetna arc section presented in the SOM. The spheres were 50 kg/m^3 denser than the surrounding mantle, which is appropriate for the "missing" ultramafic cumulates from the Talkeetna section (*19*). The downwelling instabilities generated small-scale return flow with a strong arc-parallel component (Fig. 2B). Trench-parallel transport was strongest in the regions of upwelling return flow, and there was a sharp transition between arc-normal flow in the back-arc and trench-parallel flow directly beneath the arc (Fig. 2B).

As a proxy for the orientation of seismic anisotropy arising from this flow field, we calculated the maximum elongation direction of the strain-rate ellipsoid (*22*). These calculations showed regions of coherent trench-parallel shear above zones of upwelling and radial patterns of shear located over zones of downwelling (Fig. 2C). The back-arc mantle was characterized by trench-normal shear. These results are consistent with the spatial pattern of anisotropy observed in shear-wave splitting measurements on local *S* phases from many subduction zones (*8*–*10*). Furthermore, our numerical results are also consistent with preserved fabrics in residual peridotites at the base of the Talkeetna section, which record trench-parallel flow rather than B-type olivine fabric (*23*).

Our model predicts trench-normal shear in the fore-arc, where some shear-wave splitting studies show trench-parallel fast polarization directions (*6*). There are several possible explanations for this discrepancy. First, in our model, instabilities are not advected trenchward with the corner flow. Thus, their influence on flow is imposed to be greatest directly below the arc. Second, although the development of B-type fabric is inconsistent with high temperatures directly below the arc, it is more likely in the colder fore-arc mantle (*14*). Finally, high-temperature fabrics produced under the arc could migrate into the fore-arc during subduction erosion.

To estimate the range of conditions over which foundering dominates the pattern of anisotropy, we compared the horizontal shear strain rate generated by Stokes flow to that from

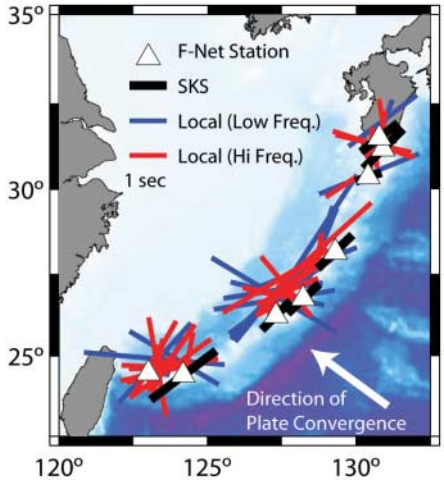

Fig. 1. Shear-wave splitting measurements from teleseismic *SKS* (thick bars) and local *S* phases (thin bars) along the Ryukyu arc (*7*, *8*). The orientation of the bars corresponds to the fast polarization direction, and bar length is scaled by delay time. Triangles denote the location of F-Net seismic stations. Splitting values for *SKS* phases are plotted at the station; values for local *S* phases are shown at the midpoint between the station and the event. Although the *SKS* measurements show relatively uniform trench-parallel fast polarization directions, the local *S* phases show a more complex pattern of anisotropy.

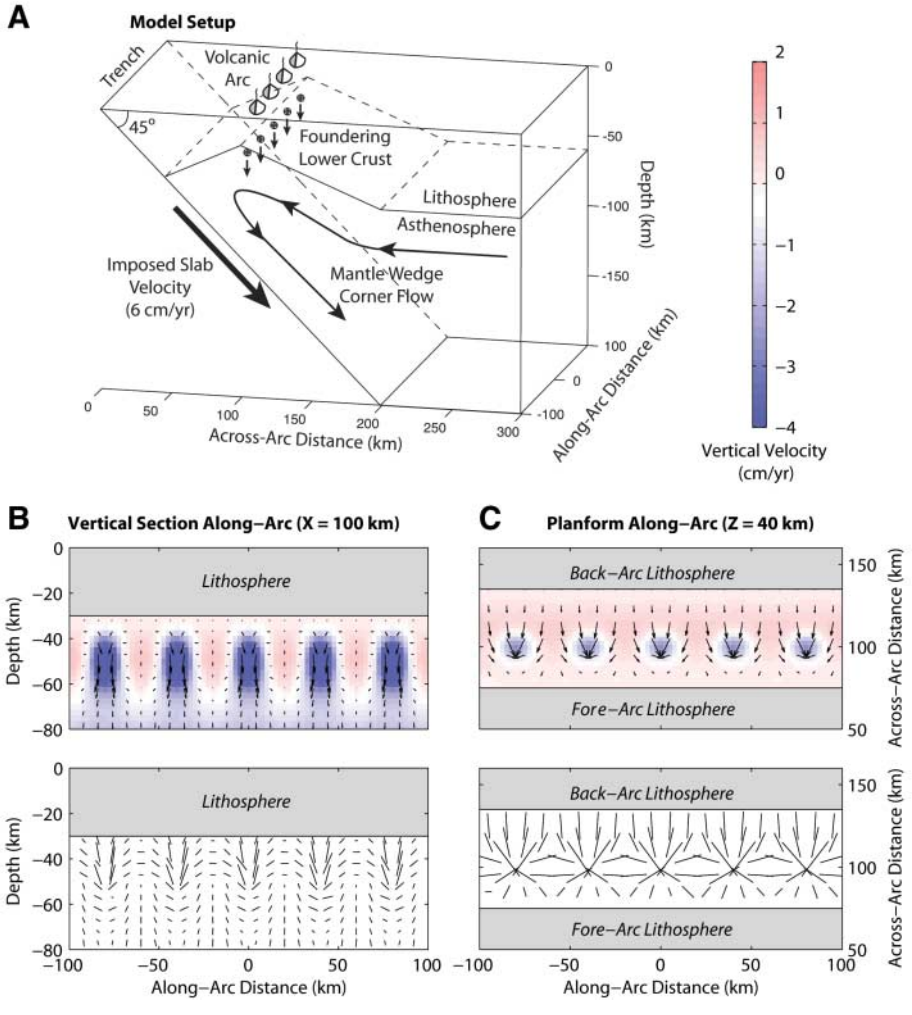

Fig. 2. (**A**) Numerical model setup for 3D calculations of mantle flow. (**B**) Vertical and (**C**) planform sections showing the orientation of the mantle velocities (top) and the long axis of the finite strain-rate ellipsoid (bottom). Foundering produces 3D flow in the mantle wedge and coherent regions of trench-parallel shear below the volcanic arc.

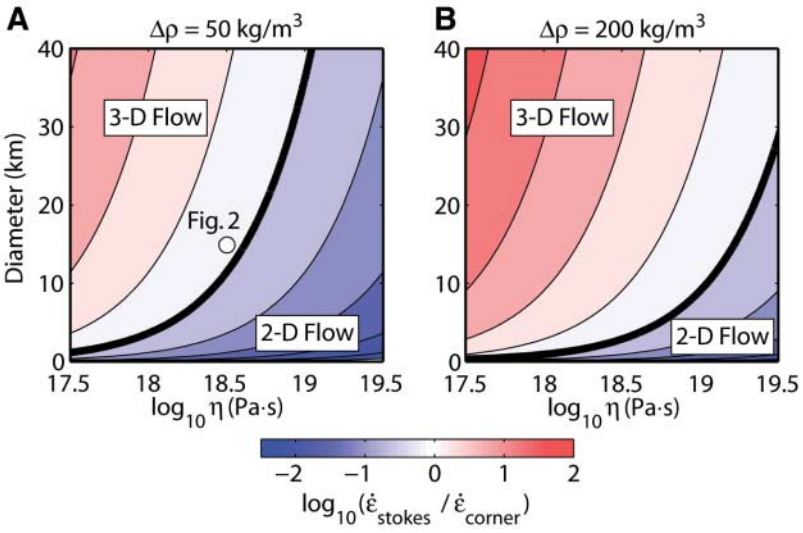

Fig. 3. Ratio of the maximum horizontal shear strain rate generated by Stokes flow, $\dot{\varepsilon}_{Stokes}$, to the mean horizontal shear strain rate associated with slab-driven corner flow, $\dot{\varepsilon}_{corner}$. Calculations are shown as a function of sphere diameter versus asthenospheric viscosity, η, assuming a slab velocity of 6 cm/year. The density contrasts relative to the surrounding mantle (Δρ) shown are appropriate for (**A**) ultramafic [(Δρ) = 50 kg/m^3] and (**B**) garnet-rich gabbroic (Δρ = 200 kg/m^3) cumulates from the Talkeetna section (*19*). For typical geologic conditions, the horizontal shear strain rates associated with Stokes flow are larger than those for corner flow, implying that lower-crustal foundering may be an important mechanism for generating 3D flow in the mantle wedge. The open circle illustrates conditions used in the 3D flow model shown in Fig. 2.

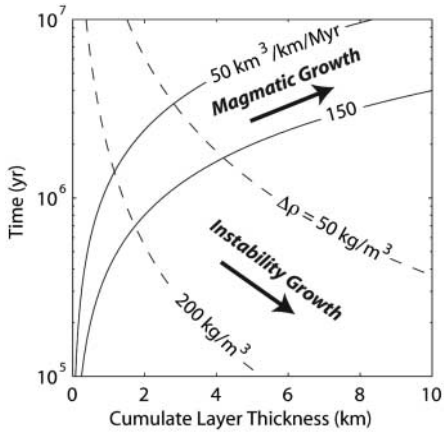

Fig. 4. Dense-layer thickness versus time, assuming magmatic fluxes of 50 to 150 km^3/km per My (solid lines). Growth rate is calculated assuming that 50% of the total magmatic flux forms a dense layer at the base of the crust. Dashed lines show instability time calculated after (*18*) as a function of cumulate layer thickness, assuming a 800°C Moho temperature for density contrasts of 50 and 200 kg/m^3 (fig. S1). For a density contrast appropriate for the missing ultramafic cumulates in the Talkeetna section (Δρ = 50 kg/m^3) and an arc flux between 50 and 150 km^3/km per My, the dense layer will grow to a thickness of ~2 to 4 km before becoming unstable.

slab-driven corner flow for a fluid of constant viscosity. The corner flow strain rate was calculated assuming a 30-km-thick lithosphere at a distance of 100 km from the trench, corresponding to the typical location of an island arc for a slab dip of 45°. Our calculations (Fig. 3) indicate that for a range of geologic conditions (for example, instability diameters of 10 to 20 km and wedge viscosities of 10^{18} to 10^{19} Pa·s), the horizontal shear strains will be strongly influenced by foundering (Figs. 2 and 3).

For foundering to affect the time-averaged flow field in the mantle wedge, the instability growth rate must be roughly balanced by the rate of crustal accretion. The rate of magma production for arcs is ~50 to 150 km^3/km per million years (My) (*24*). Assuming that about half of the magmatic flux forms a dense layer at the base of the crust (*25*), ~2 km would be added to a 30-km-wide arc every ~10^6 years (Fig. 4). The instability time for a dense layer 2 to 4 km thick is ~10^6 years at conditions appropriate for arc lower crust (Fig. 4) (*18*). These rates imply that the dense layer would grow to a thickness of 2 to 4 km over several million years before becoming unstable (intersection of solid and dashed curves in Fig. 4). Thus, we infer that instabilities with diameters of 16 to 20 km (corresponding to dense-layer thicknesses of 2 to 4 km) should form every 10^6 to 10^7 years.

Volcanic centers move within arcs on a time scale of ~10^6 years. The initiation of instabilities will probably occur between active volcanoes where igneous crust cools to <850°C near the Moho (*18*). Instability growth in these locations will in turn drive upwelling in the intervening regions. Such upwelling has the potential to induce pressure-release melting, which would in turn generate additional volcanism. Assuming 1% melt per kilobar of decompression, removing a 1- to 2-km cumulate layer over the source region for the instability will produce a minimum of ~10 km^3 of melt per instability. This process could persist through time, resulting in alternating periods of magmatic activity at arc volcanoes. An analogous process that could produce similar horizontal strains in the mantle wedge and localization of arc volcanism is upward transport of low-density diapirs composed of subducted sediment, serpentinite, and/or partial melt rising from the slab (*26*, *27*). In conclusion, the effects of 3D mantle flow induced by foundering can produce coherent regions of trench-parallel anisotropy, as well as the more complicated spatial patterns of anisotropy observed at arcs where data of higher-density shear-wave splitting data are available (*8*–*10*). Furthermore, our analysis suggests that using splitting data solely at island stations biases the interpretation of the flow field in the mantle wedge beneath the arc.

References and Notes

1. C. J. Wolfe, S. C. Solomon, *Science* **280**, 1230 (1998).
2. D. K. Blackman, J.-M. Kendall, *Geochem. Geophys. Geosys.* **3**, 10.1029/2001GC000247 (2002).
3. A. Nicolas, N. I. Christensen, in *Composition, Structure and Dynamics of the Lithosphere-Asthenosphere System*, K. Fuchs, C. Froideveaux, Eds. [American Geophysical Union (AGU) Geodynamics Series, AGU, Washington, DC, 1987], vol. 16, pp. 111–123.
4. R. M. Russo, P. G. Silver, *Science* **263**, 1105 (1994).
5. G. P. Smith *et al.*, *Science* **292**, 713 (2001).
6. J. Nakajima, A. Hasegawa, *Earth Planet. Sci. Lett.* **225**, 365 (2004).
7. M. D. Long, R. D. van der Hilst, *Phys. Earth Planet. Inter.* **151**, 206 (2005).
8. M. D. Long, R. D. van der Hilst, *Phys. Earth Planet. Inter.* **155**, 300 (2006).
9. D. L. Abt *et al.*, *Eos* **86** (Fall Meeting Suppl.), abstract T31D-05 (2005).
10. S. H. Pozgay, D. A. Wiens, H. Shiobara, H. Sugioka, *Eos* **86**, T53A-1411 (2005).
11. C. E. Hall, K. M. Fischer, E. M. Parmentier, D. K. Blackman, *J. Geophys. Res.* **105**, 28 (2000).
12. I. Katayama, H. Jung, S. Karato, *Geology* **32**, 1045 (2004).
13. I. Katayama, S.-I. Karato, *Phys. Earth Planet. Inter.* **157**, 33 (2006).
14. E. A. Kneller, P. E. van Keken, S.-I. Karato, J. Park, *Earth Planet. Sci. Lett.* **237**, 781 (2005).
15. C. Kincaid, R. W. Griffiths, *Nature* **425**, 58 (2003).
16. R. W. Kay, S. M. Kay, *Geol. Rundsch.* **80**, 259 (1991).
17. P. B. Kelemen, J. L. Rilling, E. M. Parmentier, L. Mehl, B. R. Hacker, in *Inside the Subduction Factory*, J. Eiler, Ed. (Geophysical Monograph 138, AGU, Washington, DC, 2003), pp. 293–311.
18. M. Jull, P. B. Kelemen, *J. Geophys. Res.* **106**, 6423 (2001).
19. M. D. Behn, P. B. Kelemen, *J. Geophys. Res.* **111**, 10.1029/2006JB004327 (2006).
20. G. Hirth, D. L. Kohlstedt, in *Inside the Subduction Factory*, J. Eiler, Ed. (Geophysical Monograph 138, AGU, Washington, DC, 2003), pp. 83–105.
21. P. E. van Keken, B. Kiefer, S. M. Peacock, *Geochem. Geophys. Geosys.* **3**, 10.1029/2001GC000256 (2002).
22. M. D. Behn, C. P. Conrad, P. G. Silver, *Earth Planet. Sci. Lett.* **224**, 259 (2004).

23. L. Mehl, B. R. Hacker, G. Hirth, P. B. Kelemen, *J. Geophys. Res.* **108**, 10.1029/2002JB002233 (2003).
24. B. R. Jicha, D. W. Scholl, B. S. Singer, G. M. Yogodzinski, S. M. Kay, *Geology* **34**, 661 (2006).
25. C.-T. Lee, X. Cheng, U. Horodyskyj, *Contrib. Min. Petrol.* **151**, 222 (2006).
26. P. B. Kelemen, K. Hanghøj, A. R. Greene, in *The Crust*, R. L. Rudnick, Ed. (Elsevier-Pergamon, Oxford, 2003), vol. 3, pp. 593–659.
27. T. V. Gerya, D. A. Yuen, *Earth Planet. Sci. Lett.* **212**, 47 (2003).
28. We thank M. Long, E. Kneller, and C. Conrad for conversations that motivated this work. Funding was provided by NSF grants EAR-9910899, EAR-0125919, and EAR-0509882.

Supporting Online Material
www.sciencemag.org/cgi/content/full/317/5834/108/DC1
SOM Text
Figs. S1 and S2
References

13 February 2007; accepted 9 May 2007
10.1126/science.1141269

Ancient Biomolecules from Deep Ice Cores Reveal a Forested Southern Greenland

Eske Willerslev,[1]* Enrico Cappellini,[2] Wouter Boomsma,[3] Rasmus Nielsen,[4] Martin B. Hebsgaard,[1] Tina B. Brand,[1] Michael Hofreiter,[5] Michael Bunce,[6,7] Hendrik N. Poinar,[7] Dorthe Dahl-Jensen,[8] Sigfus Johnsen,[8] Jørgen Peder Steffensen,[8] Ole Bennike,[9] Jean-Luc Schwenninger,[10] Roger Nathan,[10] Simon Armitage,[11] Cees-Jan de Hoog,[12] Vasily Alfimov,[13] Marcus Christl,[13] Juerg Beer,[14] Raimund Muscheler,[15] Joel Barker,[16] Martin Sharp,[16] Kirsty E. H. Penkman,[2] James Haile,[17] Pierre Taberlet,[18] M. Thomas P. Gilbert,[1] Antonella Casoli,[19] Elisa Campani,[19] Matthew J. Collins[2]

It is difficult to obtain fossil data from the 10% of Earth's terrestrial surface that is covered by thick glaciers and ice sheets, and hence, knowledge of the paleoenvironments of these regions has remained limited. We show that DNA and amino acids from buried organisms can be recovered from the basal sections of deep ice cores, enabling reconstructions of past flora and fauna. We show that high-altitude southern Greenland, currently lying below more than 2 kilometers of ice, was inhabited by a diverse array of conifer trees and insects within the past million years. The results provide direct evidence in support of a forested southern Greenland and suggest that many deep ice cores may contain genetic records of paleoenvironments in their basal sections.

The environmental histories of high-latitude regions such as Greenland and Antarctica are poorly understood because much of the fossil evidence is hidden below kilometer-thick ice sheets (*1*–*3*). We test the idea that the basal sections of deep ice cores can act as archives for ancient biomolecules.

[1]Centre for Ancient Genetics, University of Copenhagen, Denmark. [2]BioArch, Departments of Biology and Archaeology, University of York, UK. [3]Bioinformatics Centre, University of Copenhagen, Denmark. [4]Centre for Comparative Genomics, University of Copenhagen, Denmark. [5]Max Planck Institute for Evolutionary Anthropology, Germany. [6]Murdoch University Ancient DNA Research Laboratory, Murdoch University, Australia. [7]McMaster Ancient DNA Center, McMaster University, Canada. [8]Ice and Climate, University of Copenhagen, Denmark. [9]Geological Survey of Denmark and Greenland, Denmark. [10]Research Laboratory for Archaeology and the History of Art, University of Oxford, UK. [11]Department of Geography, Royal Holloway, University of London, UK. [12]Department of Earth Sciences, University of Oxford, UK. [13]Paul Scherrer Institut (PSI)/Eidgenössische Technische Hochschule (ETH) Laboratory for Ion Beam Physics, Institute for Particle Physics, ETH Zurich, Switzerland. [14]Swiss Federal Institute of Aquatic Science and Technology (EAWAG), Switzerland. [15]GeoBiosphere Science Center, Lund University, Sweden. [16]Department of Earth and Atmospheric Sciences, University of Alberta, Canada. [17]Ancient Biomolecules Centre, Oxford University, UK. [18]Laboratoire d'Ecologie Alpine, CNRS Unité Mixte de Recherche 5553, Université Joseph Fourier, Boîte Postale 53, 38041 Grenoble Cedex 9, France. [19]Dipartimento di Chimica Generale e Inorganica, Università di Parma, Italy.

*To whom correspondence should be addressed. E-mail: ewillerslev@bi.ku.dk

The samples studied come from the basal impurity-rich (silty) ice sections of the 2-km-long Dye 3 core from south-central Greenland (*4*), the 3-km-long Greenland Ice Core Project (GRIP) core from the summit of the Greenland ice sheet (*5*), and the Late Holocene John Evans Glacier on Ellesmere Island, Nunavut, northern Canada (Fig. 1). The last-mentioned sample was included as a control to test for potential exotic DNA because the glacier has recently overridden a land surface with a known vegetation cover (*6*). As an additional test for long-distance atmospheric dispersal of DNA, we included five control samples of debris-free Holocene and Pleistocene ice taken just above the basal silty samples from the Dye 3 and GRIP ice cores (Fig. 1B). Finally, our analyses included sediment samples from the Kap København Formation from the northernmost part of Greenland, dated to 2.4 million years before the present (Ma yr B.P.) (*1*, *2*).

The silty ice yielded only a few pollen grains and no macrofossils (*7*). However, the Dye 3 and John Evans Glacier silty ice samples showed low levels of amino acid racemization (Fig. 1A, inset), indicating good organic matter preservation (*8*). Therefore, after previous success with permafrost and cave sediments (*9*–*11*), we attempted to amplify ancient DNA from the ice. This was done following strict criteria to secure authenticity (*12*–*14*), including covering the surface of the frozen cores with plasmid DNA to control for potential contamination that may have entered the interior of the samples through cracks or during the sampling procedure (*7*). Polymerase chain reaction (PCR) products of the plasmid DNA were obtained only from extracts of the outer ice scrapings but not from the interior, confirming that sample contamination had not penetrated the cores.

Using PCR, we could reproducibly amplify short amplicons [59 to 120 base pairs (bp)] of the chloroplast DNA (cpDNA) *rbc*L gene and *trn*L intron from ~50 g of the interior ice melts from the Dye 3 and the John Evans Glacier silty samples. From Dye 3, we also obtained 97-bp amplicons of invertebrate cytochrome oxidase subunit I (COI) mitochondrial DNA (mtDNA). Attempts to reproducibly amplify DNA from the GRIP silty ice and from the Kap København Formation sediments were not successful. These results are consistent with the amino acid racemization data demonstrating superior preservation of biomolecules in the Dye 3 and John Evans Glacier silty samples, which is likely because these samples are colder (Dye 3) or younger (John Evans Glacier) than the GRIP sample (Fig. 1A, inset). We also failed to amplify DNA from the five control samples of Holocene and Pleistocene ice taken just above the silty samples from the Dye 3 and GRIP ice cores (volumes: 100 g to 4 kg; Fig. 1B) (*7*). None of the samples studied yielded putative sequences of vertebrate mtDNA.

A previous study has shown that simple comparisons of short DNA sequences to GenBank sequences by means of the Basic Local Alignment Search Tool (BLAST) make misidentification likely (*15*). Therefore, we assigned the obtained sequences to the taxonomic levels of order, family, or genus using a new rigorous statistical approach (*7*). In brief, this Bayesian method calculates the probability that each sequence belongs to a particular clade by considering its position in a phylogenetic tree based on similar GenBank sequences. In the calculation of these probabilities, uncertainties regarding phylogeny, models of evolution, and missing data are taken into account. Sequences with >90% posterior probability of membership to a taxonomic group were assigned to that group. Additionally, a given plant taxon was only considered genuine if sequences assigned to that taxon were found to be reproducibly obtained in separate analyses (by independent laboratories for the Dye 3 sample and within the laboratory for the John Evans Glacier control sample). This strict